Unveiling defect-related Raman modes of topological phononic β-MoB$_2$ single crystal via angle-resolved polarized Raman spectra

Ming Cheng [1,2,*], Run Lv [1,2,*], Xuan Luo [1,†], Zhongzhu Jiang [1,2], Wei Wang, [1,2] Tianyang Wang, [1,2] Lanxin Liu [1,2] Nan Zhou [1], Ranran Zhang [3], Wenhai Song [1], Wenjian Lu [1,‡] and Yuping Sun [1,3,4,§]

[1]*Key Laboratory of Materials Physics, Institute of Solid State Physics, HFIPS, Chinese Academy of Sciences, Hefei 230031, China*
[2]*Science Island Branch of Graduate School, University of Science and Technology of China, Hefei 230026, China*
[3]*Anhui Province Key Laboratory of Low-Energy Quantum Materials and Devices, High Magnetic Field Laboratory, HFIPS, Chinese Academy of Sciences, Hefei 230031, China*
[4]*Collaborative Innovation Center of Advanced Microstructures, Nanjing University, Nanjing 210093, China*

As a rare topological phonon material, β-MoB$_2$ exhibits superconductivity (SC) and undergoes structural transitions when subjected to pressure or doping. This unique property makes it an intriguing platform for investigating the interplay of diverse quantum order. However, the current understanding of phonons in this material remains limited. Therefore, in this study, we employ a combination of Raman scattering and first-principle calculations to investigate the phonon properties of β-MoB$_2$. Several noteworthy observations were made during the study. (1) We identified five Raman-active modes ($3A_{1g} + 2E_g$) and two abnormal modes in β-MoB$_2$. The authenticity of the five Raman-active modes was further confirmed through angle-resolved polarized Raman spectra (ARPRS) measurements and theoretical calculations. (2) We found that all Raman spectra obtained at various temperatures exhibited symmetric Lorentzian profiles. This finding implies a weak electron-phonon coupling (EPC) strength in β-MoB$_2$. We calculated the EPC strength λ of bulk β-MoB$_2$ to be 0.37, which is significantly lower than 1.71 of superconducting α-MoB$_2$. (3) Based on ARPRS measurements and the phonon dispersion, we attributed the origin of the two abnormal modes to structural distortions with regard to B atom layers of β-MoB$_2$. This research provides a foundation for exploring the relationship between defect structures and various intriguing physical phenomena observed in β-MoB$_2$.

I. INTRODUCTION

MgB$_2$ [1], being the first phonon-mediated superconductor that approaches the McMillan limit, has garnered considerable interest and precipitated a pervasive pursuit for boride superconductors with high superconducting transition temperature (T_c) [2,3]. Extensive investigations have been conducted on metal diborides MB$_2$ (M is metal), which possess lattice structures similar to MgB$_2$ [4]. However, only few of them were found to be superconductors, such as NbB$_2$ [5] and ScB$_2$ [6]. Despite this, several other intriguing physical properties have emerged in some MB$_2$ materials. According to the theoretical calculation, a portion of MB$_2$ were promising candidates for realizing topological nodal-line semimetals [7,8], including TiB$_2$, AlB$_2$, ZrB$_2$, HfB$_2$, etc. The existence of topological nodal-line fermions in TiB$_2$, AlB$_2$, and ZrB$_2$ has been confirmed through angle-resolved photoemission spectroscopy [9–12]. Furthermore, extremely large magnetoresistance has been found in ZrB$_2$ [13] and HfB$_2$ [14]. On the other hand, some rare-earth diborides have demonstrated complex magnetic phase transitions accompanied by significant changes in magnetic entropy [15,16], indicating their potential as candidate materials for magnetocaloric applications.

MoB$_2$, belonging to the MB$_2$ compound system, exhibits two distinct crystal structures depending on the stoichiometry of B atoms: a hexagonal AlB$_2$-type structure (α phase) with the $P6/mmm$ space group and a rhombohedral structure (β phase) with the $R\bar{3}m$ space group [17]. β-MoB$_2$ is a natural topological phonon material that has been investigated using inelastic x-ray scattering measurements [18]. Similar to topological electronic materials, the nontrivial band structure of phonons gives rise to phonon surface states [19]. These surface states exhibit robustness against local defects and are likely to induce electric anomalies on the surface through electron-phonon coupling (EPC) [19]. Additionally, recent studies have demonstrated that β-MoB$_2$ exhibits superconductivity (SC) under pressure, with a critical pressure of approximately 20 GPa and a structural transition occurring at around 70 GPa, accompanied by a T_c approximately 32 K [20]. Subsequent theoretical investigations have explored the potential origins of SC in α-MoB$_2$ at 70 GPa [21,22].

---

*These authors contributed equally to this work.
†xluo@issp.ac.cn
‡wjlu@issp.ac.cn
§ypsun@issp.ac.cn

However, the superconducting behavior and structural transitions in β-MoB$_2$ remain largely unknown. Moreover, previous research suggests that doping can simultaneously induce SC and structural transitions in β-MoB$_2$ [17,23,24]. Therefore, in order to gain a comprehensive understanding of the underlying mechanisms behind the diverse physical phenomena in β-MoB$_2$ and their interplay, further investigation of the phononic properties is warranted.

Raman spectroscopy, a valuable analytical technique, is employed to elucidate the vibrational characteristics of crystal structures (i.e., phonons). Initially, Raman scattering plays a pivotal role in uncovering the underlying causes of structural transitions in low-dimensional materials [25–27]. For instance, extensive analysis of the Raman spectra revealed that the space group of IrTe$_2$ differs from the initially predicted $P\bar{3}m1$, instead presenting as $P\bar{3}c1$ at room temperature. Additionally, Raman scattering is extensively employed for investigating defects in various materials [28–30].

Furthermore, Raman spectroscopy proves to be a valuable technique in assessing the strength of coupling between discrete phonon states and continuum states. Typically, the Raman spectra exhibit a symmetrical Lorentzian profile. However, when the phonons of certain materials couple with quasiparticles, the symmetrical Lorentzian profile transforms into an asymmetrical Fano profile, which can be effectively fitted using the Fano function. The parameter q in the Fano function is often employed to gauge the intensity of electron-quasiparticle coupling. This phenomenon has been extensively documented in the context of superconductors, charge-density wave (CDW) materials, and magnetic materials [31–35].

Additionally, Raman scattering represents a valuable means of investigating the presence of surface or interface phonons. The first documented instance of surface phonons was the observation of Sb vibration on the (110) surface of III-V semiconductors, namely, InP, GaAs, and GaP [36]. The reduced symmetry of this configuration renders the phonons Raman active, thus indicating their ordered arrangement on the semiconductor substrate. Subsequently, the presence of surface phonons was successfully detected through Raman spectroscopy in the case of the topological insulator Bi$_2$Se$_3$ [37]. In scenarios where a gap exists within the phonon density-of-state (DOS), the surface phonon DOS becomes distinct from that of the bulk, showing significant distortion. In Bi$_2$Se$_3$ single crystals, aside from four Raman-active bulk phonons, six additional modes were observed with intensities approximately 20–100 times weaker than those of the bulk phonons. Moreover, recent advancements have revealed the possibility of first-order Raman scattering originating from surface optical phonons resulting from reduced symmetry at the surface of pristine metals [38].

Therefore, Raman scattering proves to be a valuable tool for investigating several key aspects pertaining to β-MoB$_2$. First, it allows us to address the question of whether topological surface phonons can be observed through Raman scattering. Second, if these topological phonons are indeed measurable, it raises the inquiry of whether they exhibit Fano resonance caused by strong EPC. Third, Raman scattering facilitates the assessment of the intensity of EPC within the nonsuperconductive β-MoB$_2$ phase. Fourth, it provides us

more phononic information to understand SC of β-MoB$_2$ under low pressure.

In this study, we conducted a comprehensive investigation on phonons of β-MoB$_2$ single crystals. The ac plane of the β-MoB$_2$ revealed the presence of five Raman-active modes ($3A_{1g} + 2E_g$) along with two additional modes. The symmetry of these modes were characterized via detailed measurements of angle-resolved polarized Raman spectra (ARPRS). And we found that these two additional modes shared the same symmetry with two adjacent A_{1g} modes. Combining with theoretical calculations, these A_{1g} modes were mainly concerned with the vibration of B atoms. Additionally, we studied the temperature dependence of these modes. No new modes or strong EPC-induced Fano profile were observed at low temperatures. Moreover, we calculated the EPC strength of β-MoB$_2$ to be 0.37 and found that it was mainly contributed by low-frequency acoustic phonons. Finally, we discussed the origin of two modes and considered that they were more likely to be associated with the defect structure in B atom layers of β-MoB$_2$.

II. METHODS

The β-MoB$_2$ single crystal was synthesized using the high temperature Al flux method, as previously described in the literature [39]. A combination of Mo powder (with a purity of 99.9%), B powder (with a purity of 99.9%), and Al powder (with a purity of 99.5%) was mixed in a molar ratio of $1 : 2.5 : 73.3$. The resulting mixture was placed into an alumina crucible, which was then put into a tubular furnace. Under a continuous flow of argon, the mixture was heated to 1500 °C and maintained at this temperature for a duration of 10 hours. Subsequently, the temperature of the tubular furnace was slowly reduced to 900 °C at a rate of 3 °C/h. The mixture was ultimately held at 900 °C for several hours before being cooled to room temperature. The excess Al flux was removed by sodium hydroxide solution, and some black shiny β-MoB$_2$ single crystals could be obtained.

β-MoB$_2$ single crystals and polycrystalline powder x-ray diffraction (XRD) measurements were performed by the PANalytical X' Pert diffractometer using the Cu K_α radiation ($\lambda = 0.15406$ nm) at room temperature. Rietveld refinement of powder XRD data was carried out by using the FULL-PROF software package [40]. The structural characterization was performed by transmission electron microscopy (TEM). Inductively coupled plasma optical emission spectroscopy (ICP-OES) measurements were performed on a Thermo iCAP 7000 SERIES instrument. Electrical transport and specific-heat measurements were performed using a Quantum Design physical property measurement system (PPMS-9T). The Raman spectra at all temperatures from 5 to 300 K were measured using an Horiba Jobin YvonT64000 Micro-Raman instrument with a laser Torus 532 nm as an excitation source in a backscattering geometry. A back-illuminated charge-coupled device cooled by liquid nitrogen was used to detect the scattered light. The ab plane and ac plane of samples were clockwise rotated 360° with a step of 15° for ARPRS measurements.

The first-principles calculations based on density-functional theory (DFT) were carried out using the
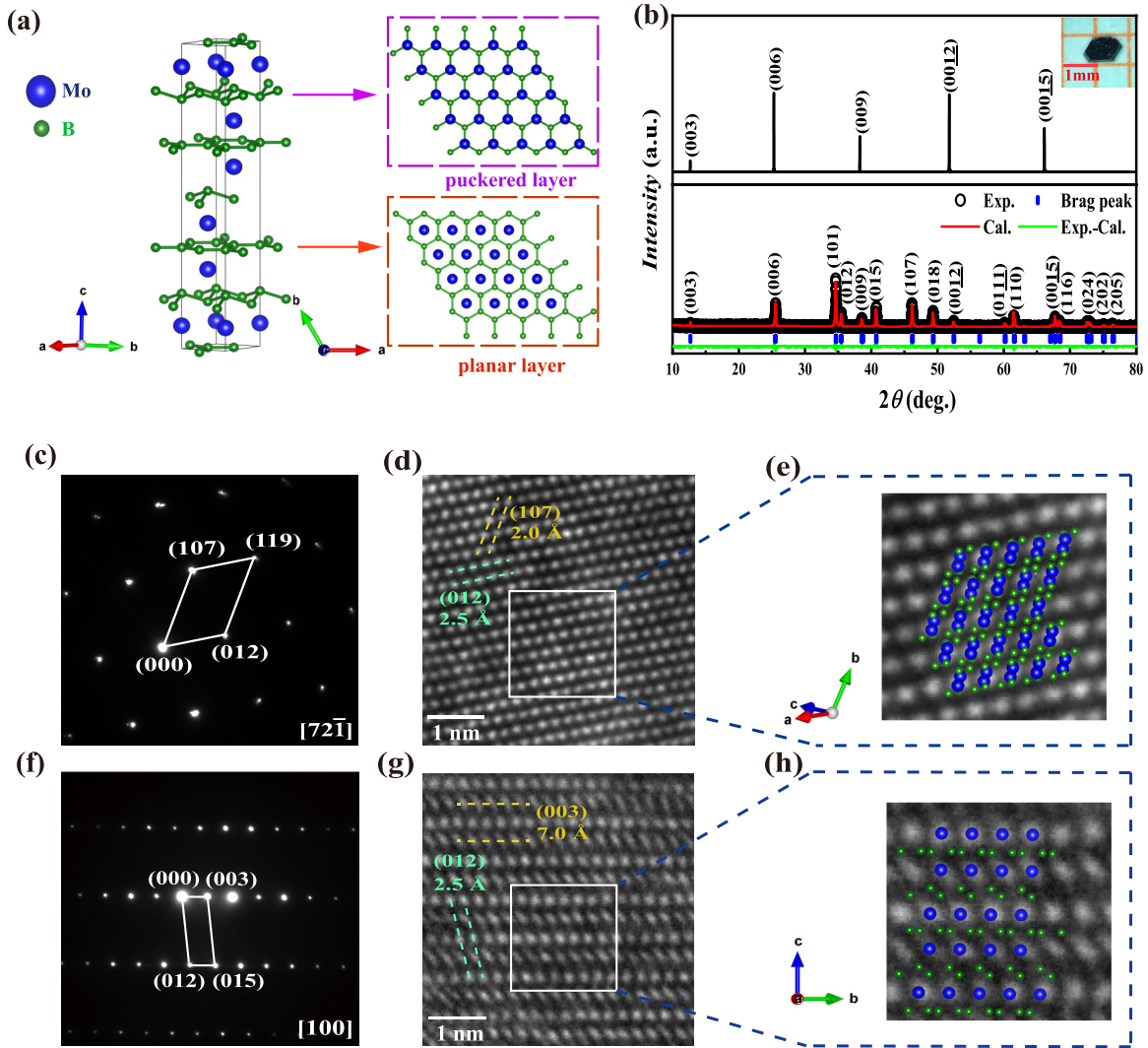
FIG. 1. (a) Crystal structures of β-MoB$_2$ observed from side view and top view. (b) The upper section is the XRD pattern of the single crystal measured on the (00*l*) surface. The inset presents the typical crystal size is about $0.8 \times 0.8 \times 0.1$mm^3. The lower section is Rietveld refined powder XRD patterns at room temperature for crushed β-MoB$_2$ crystals. The vertical marks (blue bars) stand for the position of the Bragg peaks, and the solid line (green line) at the bottom corresponds to the difference between experimental and calculated intensities. The SAED patterns of β-MoB$_2$ single crystal taken along (c) [72$\bar{1}$] and (f) [100]. HRTEM images of the (d) β-MoB$_2$ (72$\bar{1}$) and (g) (100) facets. Scale bar is 1 nm. Enlarged HRTEM images of the (e) β-MoB$_2$ (72$\bar{1}$) and (h) (100) facets denoted by the white box with corresponding crystal structure.

Vienna *ab initio* simulations package (VASP) [41]. The interaction between the electrons and ionic cores was treated by the projector augmented wave (PAW) method [42]. The exchange-correlation interaction was described by the generalized gradient approximation (GGA) and parametrized by the Perdew-Burke-Ernzerhof functional [43]. The plane-wave energy cutoff was set to 500 eV. The Gaussian smearing method was used to calculate the charge density with a smearing parameter of $\sigma = 0.1$ eV. The Brillouin zone (BZ) was sampled with a $13 \times 13 \times 13$ Monkhorst-Pack (MP) *k*-point mesh. The structure was fully relaxed with total-energy convergence of 10^{-8} eV and the Hellmann-Feynman force acting on each atom is less than 5×10^{-4} eV/Å. The phonon dispersion was calculated by using density-functional perturbation theory (DFPT) as implemented in VASP and the phonon frequency was

determined via the PHONOPY code [44] with a $2 \times 2 \times 2$ supercell and a $5 \times 5 \times 5$ mesh of *k* points. The EPC was calculated using the DFPT method as implemented in the QUANTUM ESPRESSO (QE) package [45], using a $5 \times 5 \times 5$ mesh of *q* points and a $20 \times 20 \times 20$ mesh of *k* points.

III. RESULTS AND DISCUSSION

The structure of β-MoB$_2$ single crystal is shown in Fig. 1(a); a continuous network of six membered rings formed by metal atoms and B atoms alternately stack along the *c* axis of crystal coordinates. To be specific, the layers formed by B atoms consist of planar layers and puckered layers, metal atoms are located above the center of every six-membered ring formed by B atoms for planar layers and above the lattice point for puckered layers. The XRD patterns of β-MoB$_2$
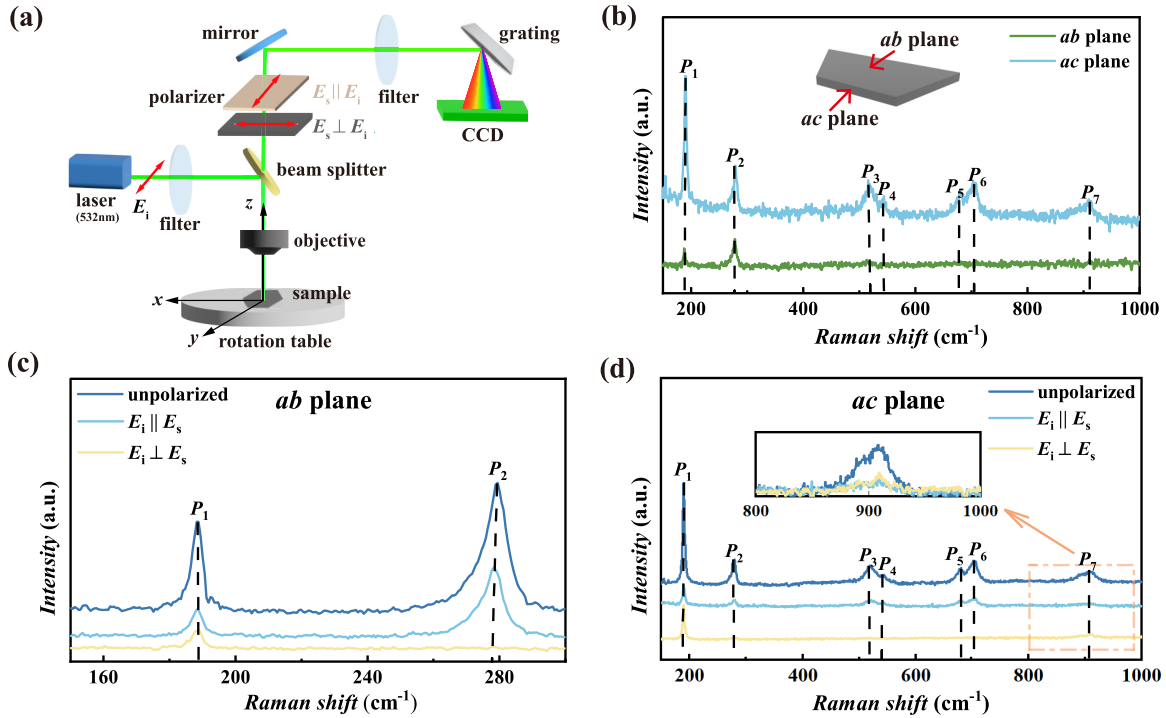
FIG. 2. (a) Schematic diagram of Raman measurement setup. (b) Raman spectra measured on the *ab* plane (green line) and the *ac* plane (blue line) at room temperature. Raman spectra of β-MoB$_2$ under the unpolarized configuration, parallel-polarized configuration [$z(xx)\bar{z}$, i.e., $E_i \parallel E_s$] and the cross-polarized configuration [$z(xy)\bar{z}$, i.e., $E_i \perp E_s$] on the (c) *ab* plane and (d) *ac* plane. The inset of panel (d) shows the enlarge of high-frequency region denoted by the orange square icon

single crystals are presented in the upper section of Fig. 1(b), with an optical image of a representative single crystal in the inset. The observed XRD peaks exclusively correspond to the (00*l*) crystallographic planes, indicating that the exposed surface of the single crystal is the *ab* plane. To further validate the crystal structure, a Rietveld structure refinement of the powder XRD data was performed on crushed single crystals at room temperature, as depicted in the lower section of Fig. 1(b). The refined lattice parameters were determined to be $a = b = 3.013$ Å and $c = 20.94$ Å, which exhibits excellent agreement with previously reported values [18]. Additionally, the elemental composition of the crystals was analyzed using ICP, confirming a Mo : B ratio of 1 : 2.15.

To characterize the structure of β-MoB$_2$, the high-resolution TEM (HRTEM) images of the $(72\bar{1})$ [Fig. 1(d)] and (100) [Fig. 1(g)] facets of exfoliated β-MoB$_2$ nanosheets were obtained. The selected-area electron diffraction (SAED) patterns of the observed areas are presented in Figs. 1(c) and 1(f), demonstrating the uniformly distributed diffraction spots that confirm the single-crystal nature. The detailed analysis of the crystal structure on two planes is demonstrated by the magnified HRTEM images with corresponding crystal structure of the areas indicated by white boxes in Figs. 1(e) and 1(h).

Figure 2(a) displays the schematic diagram of Raman measurements setup along the *ac* projected plane. E_i and E_s represent the polarization direction of the incident laser and the scattering beam, respectively. It should be noted that the polarization of incident laser beam was fixed and the polarization of the scattered beam was changed by using a parallel (reddish) and a cross (gray) polarizer, which was utilized for

the parallel ($E_i \mathbin{/\mkern-5mu/} E_s$) and perpendicular ($E_i \perp E_s$) configurations, respectively. In addition, the sample was placed on a rotation table in order to complete the following ARPRS measurements [46–48]. The Raman spectra were acquired by conducting measurements on the basal plane and the edge plane of β-MoB$_2$ single crystal. The lattice parameter of β-MoB$_2$ *a* is equal to *b*, so the *ac* plane is equivalent to the *bc* plane. In this context, we refer to the basal plane as the *ab* plane and the edge plane as the *ac* plane. Room-temperature Raman spectra obtained from the two planes of the sample are shown in Fig. 2(b). The *ab* plane exhibits two prominent peaks at energies of 191.0 cm^{-1} (P_1) and 279.3 cm^{-1} (P_2), aligning with previous observations in the literature [20]. In contrast, the *ac* plane reveals the presence of five distinct peaks at energies of 519.6 cm^{-1} (P_3), 541.2 cm^{-1} (P_4), 679.8 cm^{-1} (P_5), 703.9 cm^{-1} (P_6), and 905.1 cm^{-1} (P_7). The inconsistent number of peaks on these two planes may be attributed to variations in the Raman-scattering cross section.

Based on the fundamental principles of momentum and energy conservation, it is determined that only the optical phonons specifically located at the center of the Brillouin zone (Γ point) participate in the first-order Raman-scattering process. The irreducible presentations of phonon modes at the Γ point of β-MoB$_2$ based on its crystal point group D_{3d} are as follows: $\Gamma_{MoB_2} = 3A_{1g} + 3E_g + 3E_u + 3A_{2u}$. Among these representations, the ($E_u + A_{2u}$) modes correspond to acoustic phonons, while the ($2E_u + 2A_{2u}$) modes are inactive and do not contribute to Raman scattering. On the other hand, the remaining six modes ($3A_{1g} + 3E_g$) correspond to active optical phonons which are involved in the Raman-scattering process. Therefore, based on this analysis, it is expected that
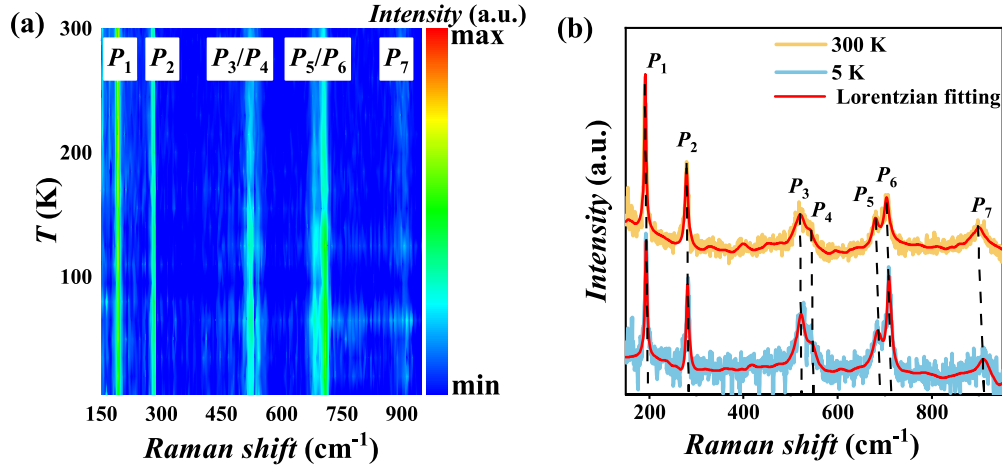
FIG. 3. (a) Contour map of Raman spectra of β-MoB$_2$ measured on the ac plane from 5 to 300 K with a step of 15 K. (b) The Raman spectra measured at 5 and 300 K. The solid line is the fitting to the Lorentzian function.

our experimental measurements would exhibit no more than six modes. However, it was observed that the actual number of peaks detected was seven, surpassing the expected results derived from symmetry analysis.

Figures 2(c) and 2(d) depict the polarized-dependent Raman spectra collected from two planes. The inset of Fig. 2(d) provides an enlarged view of the high-frequency region indicated by an orange dotted box, which highlights the consistent intensity of P_7 under two different configurations. In most cases, A_{1g} modes can be observed in the parallel-polarized configuration, whereas doubly generated E_g modes can be found in the both parallel-polarized and cross-polarized configurations. So the assignment of peaks P_1 and P_7 to E_g modes and the remaining five peaks to A_{1g} modes was determined through polarized Raman spectra measurements.

Temperature is a critical parameter that influences the crystal structure and topological properties, so we also measured temperature-dependent Raman spectra on the ac plane of the sample within a temperature range of 5 to 300 K, with a step interval of 15 K, as depicted in Fig. 3. Remarkably, no significant changes were observed in the Raman spectra throughout the entire temperature range [Figs. 3(a) and 3(b)], indicating the absence of any concealed structural transitions. Additionally, all peaks exhibited Lorentzian profiles, suggesting weak EPC for the Raman-active phonons detected experimentally, even at low temperatures (5 K). A detailed analysis can be seen in Appendix B.

To gain further insights into the Raman spectra, we conducted first-principles calculations and adopted the lattice parameters of $a = b = 3.01$ Å, $c = 20.94$ Å, as determined by powder XRD data. The crystal structure of β-MoB$_2$ consists of six atoms, comprising three acoustic phonons and fifteen optical phonons. Table I summarizes the calculated and experimental phonon frequencies, while Fig. 4(c) presents the vibration patterns of all calculated optical phonons. Based on the calculated results, it is evident that the appearance of peaks P_4 and P_5 deviates from the expected behavior. Figure 4(a) shows the phonon dispersion of β-MoB$_2$, with the displacements of Mo and B atoms labeled. Notably, at the Γ point, there exists an energy gap of approximately 100 cm^{-1} between the lower optical phonon branches and the

higher optical phonon branches, which corroborates previous findings [18]. It is observed that the phonon spectrum in the low-frequency range of 0 to 263 cm^{-1} (P_1, P_2) is primarily contributed to by the heavier Mo atoms, while the higher frequency range from 366 to 911 cm^{-1} (P_3–P_7) is dominated by the lighter B atoms. After obtaining the phonon dispersion, we further evaluate the EPC strength of β-MoB$_2$. We calculated the Eliashberg spectral function $\alpha^2F(\omega)$ and EPC constant λ based on the equation [49]

$$\lambda = 2\int d\omega \alpha^2 F(\omega)/\omega. \quad (1)$$

Figure 4(b) illustrates the distribution of EPC projected onto the phonon dispersion, where the size of the red circles represents the magnitude of EPC. Remarkably, due to the relatively low DOS of B atoms near Fermi level and the high frequencies of B atom vibration modes, the contribution of B atoms to the total EPC is insignificant, similar to that in α-MoB$_2$ under high pressure [22]. Moreover, the EPC originating from phonons located at the Γ point is extremely weak, consistent with our observations in the Raman spectra. The calculated EPC strength λ is 0.37, significantly lower than the value of 1.71 reported for α-MoB$_2$ under high pressure but comparable to the calculated values for nonsuperconducting

TABLE I. Comparison of the calculated and experimental phonon frequencies at room temperature.

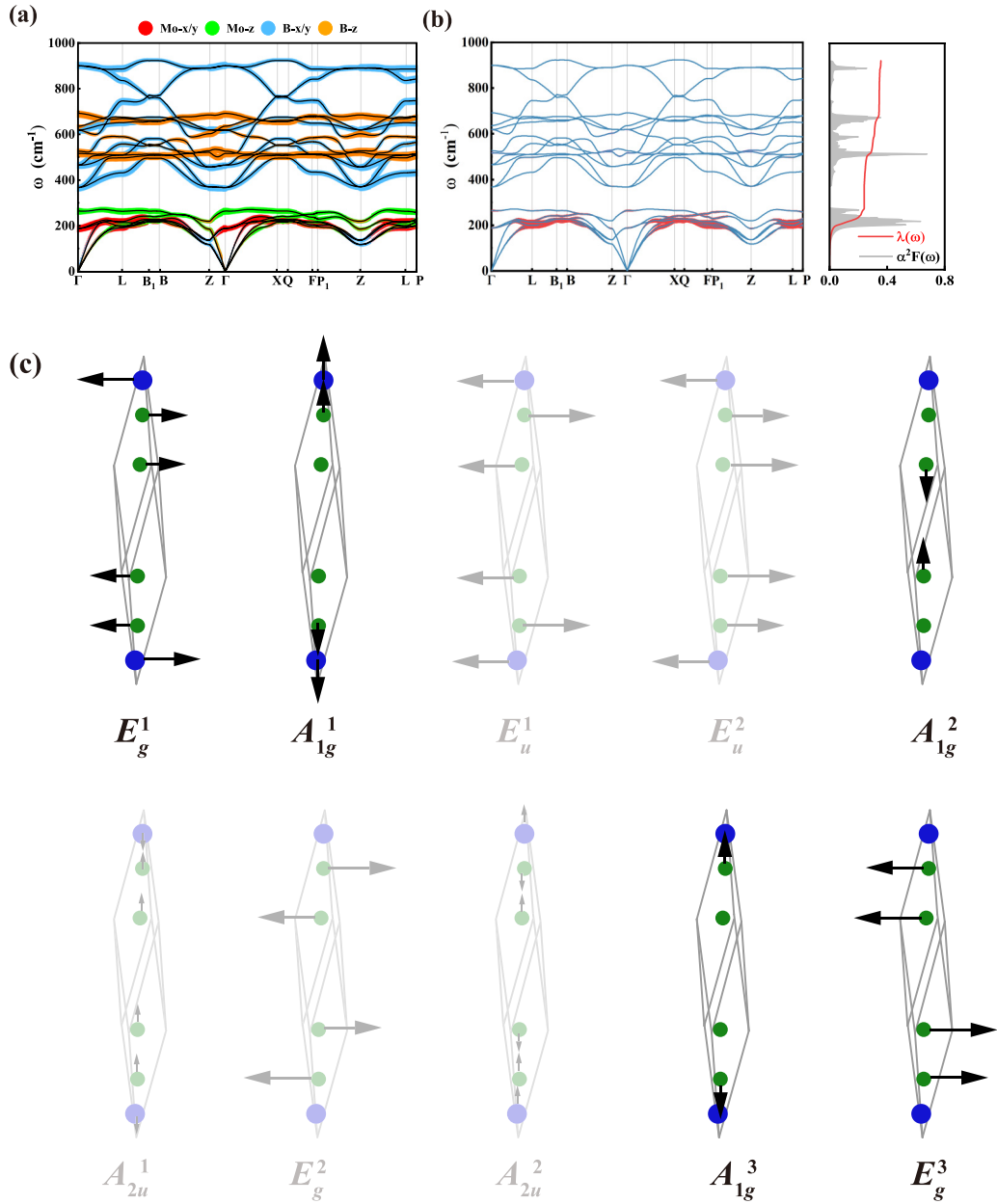| Mode	Calc. Freq. (cm^{-1})	Expt. Freq. (error) (cm^{-1})
E_g	186.92	189.95 (0.05)
A_{1g}	258.16	278.55 (0.34)
E_u	365.89	
E_u	463.23	
A_{1g}	519.77	519.60 (0.83)
A_{2u}	523.03	
E_g	616.96	
A_{2u}	633.64	
A_{1g}	689.18	703.90 (0.54)
E_g	898.60	905.14 (1.25)

FIG. 4. (a) Phonon dispersion projected on atomic in-plane (x and y) and out-of-plane (z) vibrations. (b) Phonon dispersion weighed by the magnitude of EPC strength λ_{qv} (red circle) and the Eliashberg function $\alpha^2 F(\omega)$ with integrated EPC constant $\lambda(\omega)$. (c) Calculated phonon vibration modes of optical phonons for β-MoB$_2$. The transparent patterns indicate that they have not been observed experimentally.

compounds such as VB$_2$, AlB$_2$, and YB$_2$ [4], as well as the experimental value for the weak-coupling superconductor WP [31].

To understand the origin of these two modes, further validation of the symmetry and anisotropy of these phonon modes via ARPRS measurements was necessary. Since most peaks are visible under parallel-polarized configuration, ARPRS measurements were performed under this configuration. The configuration of the ARPRS setup is illustrated in Figs. 5(a) and 5(b). The contour color maps in Figs. 5(c) and 5(f) demonstrate that the A_{1g} and E_g modes exhibit angle-independent behavior under the ab plane configurations. Furthermore, they display either twofold or fourfold symmetry under the ac plane configurations.

In general, the intensity (I) of a particular Raman-active mode can be expressed as

$$I \propto \sum_j |e_i R_j e_s|^2, \qquad (2)$$

where R_j represents Raman tensor for a particular mode, e_i and e_s represent polarization direction of incident light and scattered light with respect to laboratory coordinates, respectively. For an arbitrary Raman tensor in the corresponding crystal coordinates:

$$R_j = \begin{pmatrix} a & b & c \\ d & e & f \\ g & h & i \end{pmatrix}, \qquad (3)$$
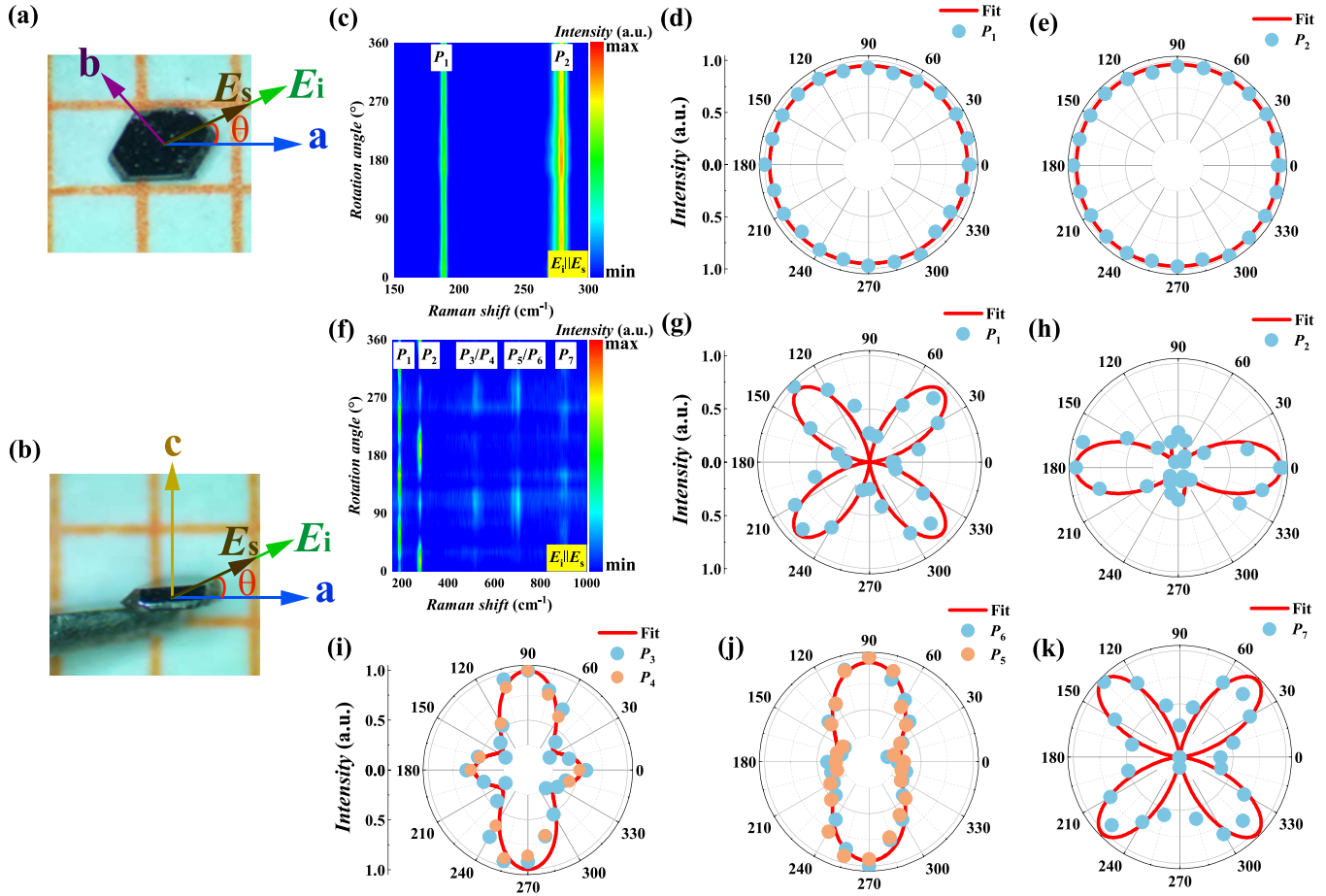
FIG. 5. ARPRS of β-MoB$_2$ single crystal. (a), (b) The sketch map of the ARPRS configurations in two planes. Contour map of measured phonon intensity as a function of angle and energy measured on the (c) ab plane and the (f) ac plane. Angle dependence of the Raman peak intensity of measured on the (d), (e) ab plane and the (g)–(k) ac plane under the parallel-polarized configuration. The blue and orange dots show the measured data and the solid line is the fitted result according to Eqs. (7a)–(7d).

when rotating the sample's ab or ac plane and the angle of rotation is θ, angle dependence of the intensity for the Raman-active mode can be expressed as [52]

$$I_{ab} \propto [e\cos^2\theta - (b+d)\cos\theta\sin\theta + a\sin^2\theta]^2, \quad (4a)$$

$$I_{ac} \propto [i\cos^2\theta + (c+g)\cos\theta\sin\theta + a\sin^2\theta]^2. \quad (4b)$$

For β-MoB$_2$, the Raman-scattering tensors corresponding to different phonon modes can be written as

$$E_g = \begin{pmatrix} 0 & -c & -d \\ -c & 0 & 0 \\ -d & 0 & 0 \end{pmatrix}, \quad \begin{pmatrix} c & 0 & 0 \\ 0 & -c & d \\ 0 & d & 0 \end{pmatrix}, \quad (5)$$

$$A_{1g} = \begin{pmatrix} a & 0 & 0 \\ 0 & a & 0 \\ 0 & 0 & b \end{pmatrix}. \quad (6)$$

Thus, the angle-dependent Raman-scattering intensities of the A_{1g} and E_g modes in two planes can be formulated as

$$ab : E_g : I \propto c^2, \quad (7a)$$

$$A_{1g} : I \propto a^2, \quad (7b)$$

$$ac : E_g : I \propto d^2\sin^2 2\theta + c^2\sin^4\theta, \quad (7c)$$

$$A_{1g} : I \propto (a\sin^2\theta + b\cos^2\theta)^2. \quad (7d)$$

As depicted in Figs. 5(d), 5(e) and 5(g)–5(k), the theoretical curves exhibit a strong agreement with the experimental data for the five experimental modes, with the exception of P_4 and P_5. This demonstrates that our symmetry analysis for each phonon is well founded and reasonable. Notably, the intensities calculated from above equations usually reach either the maximum or the minimum at 0° and 90° under parallel-polarized configuration. Therefore, the crystalline orientation of β-MoB$_2$ can be decided by APPRS measurements. Furthermore, it is important to note that the angle dependence of intensity varies among different E_g or A_{1g} modes, suggesting the presence of distinct Raman tensors for each phonon mode. Upon careful examination of Figs. 5(i) and 5(j), it can be observed that P_4 shares the same Raman tensor as P_3, while P_5 exhibits the same Raman tensor as P_6.

Integrating the information obtained from both experimental observations and theoretical calculations, we can now try to elucidate the origin of peaks P_4 and P_5. We initially explore the possibility of a topological explanation, considering that β-MoB$_2$ is classified as a topological phonon material. By comparing our phonon dispersion with the literature [18], we can directly assess the validity of this speculation based on the phonon energies. Previous studies [18] have reported the presence of two topological phonon branches at energies of
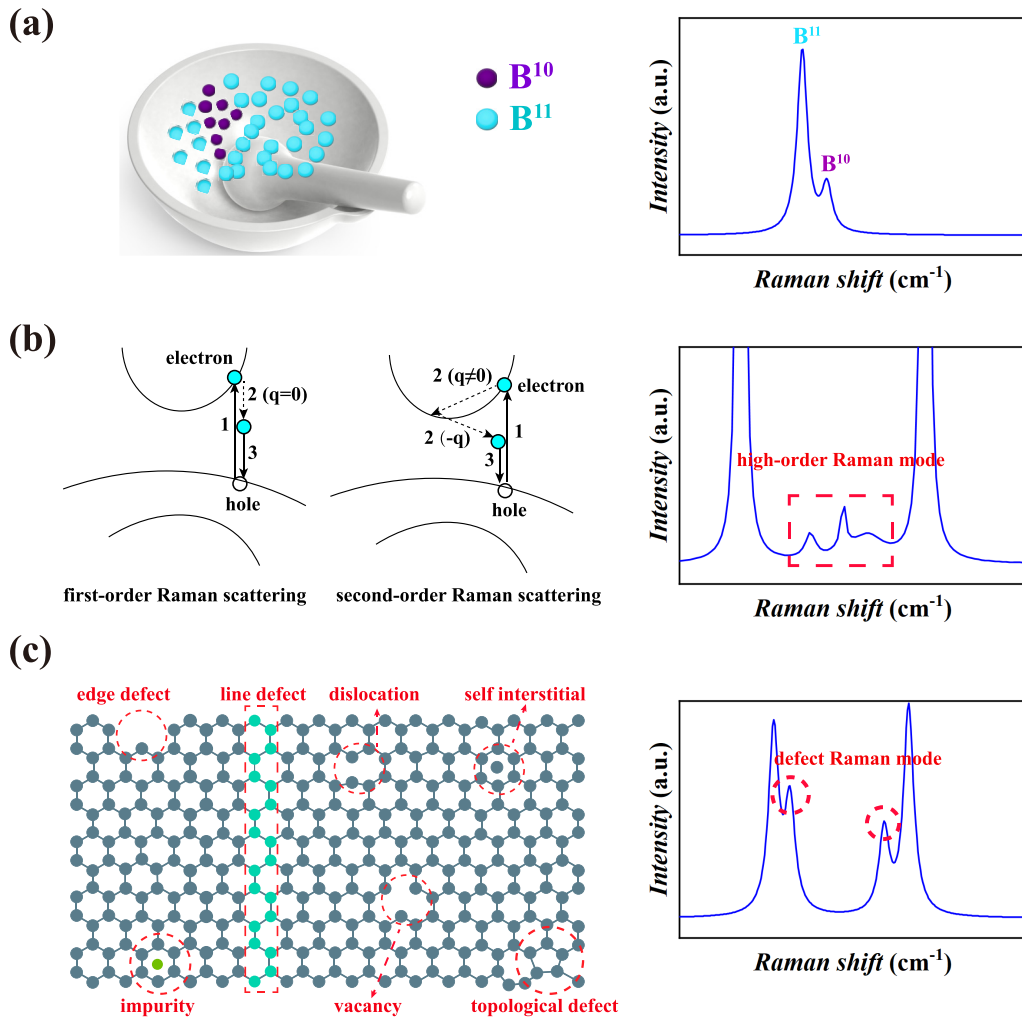
FIG. 6. Schematic picture of three origins involving in the appearance of new Raman peaks. (a) The origin of B isotopic effect. The two isotopes in the raw materials are distinguished by blue and purple balls. (b) The origin of high-order Raman scattering [50]. The three curves from top to bottom represent one conduction band and two valence bands. The numbers 1, 2, and 3 indicate the sequence of events that occur during the Raman-scattering process. The high-order Raman modes are indicated by red dashed box. (c) The origin of defect. The different types of defects present in the crystal lattice [51], as well as the Raman modes associated with defect formation, are identified by red dashed circle.

240 and 760 cm^{-1}, respectively. The observed energy of peaks P_4 and P_5 contrasts with the expected energies associated with topological phonon branches. Consequently, we can exclude the possibility of a topological origin for these peaks. Alternatively, we can explore more general explanations that often account for the appearance of new peaks or the splitting of original peaks in Raman spectra. These explanations typically attribute such phenomena to three factors: (i) the isotopic effect, (ii) high-order Raman scattering from other regions of the BZ, and (iii) symmetry breaking induced by the defect structure. A conceptual illustration of these three potential origins is presented in Fig. 6.

In materials rich in elemental B, it is not uncommon for a peak to split into two due to the presence of different B isotopes, namely, B^{10} and B^{11}, in the raw materials [53,54]. The intensity of these split peaks depends on the relative abundance of the two isotopes in the raw materials, resulting in a fixed ratio of intensity between the two peaks. In nature, the abundances of B^{11} and B^{10} are 80% and 20%,

respectively, so the intensity ratio between the split peaks originating from B isotopes should be approximately 8 : 2. However, in our experiments, their intensity ratios are measured to be approximately 12.8 : 1 and 2 : 1, respectively (see Fig. 10 in Appendix C). Thus, the origin of the isotopes can be excluded.

Furthermore, it is important to consider high-order Raman scattering, which involves the multiphonon light scattering process. Compared with first-order Raman scattering, high-order Raman scattering exhibits significantly weaker intensity and is typically observed only under resonant Raman scattering conditions which often require higher laser energy [55,56]. Due to the multitude of possible combinations and the constraints imposed by crystal symmetries, the assignment of high-order Raman peaks is a highly complex process. Notably, in our Raman spectra, the intensities of the two peaks in question are remarkably strong and comparable to those of the first-order Raman peaks, further discounting the influence of high-order scattering [origin (ii)].

Therefore, based on the above analysis, the isotopic effect and high-order Raman scattering can be ruled out as explanations for the observed phenomena, suggesting that the origin of the observed splitting may be attributed to origin (iii), namely, symmetry breaking induced by the defect structure. According to our observations, the spectral features labeled P_4 and P_5 can be attributed to A_{1g} modes, which exhibit the same Raman tensor as P_3 and P_6. This suggests that their presence is likely a result of the splitting of two A_{1g} modes induced by the defect structure. As depicted in Figs. 4(a) and 4(c), these modes correspond to out-of-plane vibrations of the B atom layers, thus indicating that their splitting originates from distortions within the B atom layers. Similar observations have been made in ReB_2 and MgB_2, where the presence of defects has been found to disrupt the Raman selection rules and give rise to additional weak peaks overlapping with the primary peaks [57,58]. Furthermore, Zhao *et al.* [59] have also reported the generation of a novel A_{1g}-like localized Raman mode induced by a Se vacancy, which possesses the same Raman tensor as the A_{1g} mode of $MoSe_2$, aligning with our observations. To confirm whether the peak splitting is induced by lattice defects, we subjected the single crystal to annealing at $900\,^\circ\mathrm{C}$ in order to minimize the local lattice distortions caused by defects. What is more, we measured the Raman spectra of two single crystals before and after annealing (see Fig. 9 in Appendix C). It can be observed that before annealing, the splitting of the two A_{1g} peaks is evident. However, after the annealing process, the peak splitting is significantly reduced, more closely approaching a single peak.

Recently, the emergence of SC in WB_2 under pressure has been reported, along with a proposed model of SC induced by local defects [60,61]. Additionally, the ratio of planar B layers has been found to play a crucial role in compressed WB_2 compared with ReB_2 under pressure [61]. In the current studies on β-MoB_2 doping [17,23,24], SC always emerges in conjunction with the appearance of the α phase. Perhaps the α phase is the only phase in the MoB_2 system that exhibits SC. So the identification of these two peaks in our measurements may contribute to understanding the relationship between the defect structure and SC in MoB_2.

In conclusion, a systematic investigation of Raman scattering was conducted on the topological phonon material β-MoB_2. The analysis revealed the presence of five Raman active modes ($3A_{1g} + 2E_g$) and two additional modes in the β-MoB_2 single crystal. These two modes exhibited the same symmetry with two adjacent A_{1g} modes via ARPRS. Temperature-dependent Raman spectra indicated that the number of Raman peaks remained unchanged and the Lorentzian profile persisted at low temperature. Electronic structure calculations and phonon spectrum calculations were performed for bulk β-MoB_2, revealing a weak EPC strength of 0.37, which is mainly contributed by acoustic phonons. Based on our theoretical and experimental findings, we proposed that the two additional modes observed in the β-MoB_2 single crystal are likely attributed to the distortion of B atom layers. This investigation provides a foundation for further exploration of the connection between defect structures and various intriguing physical phenomena in β-MoB_2.

APPENDIX A: TRANSPORT PROPERTIES OF β-MoB_2 SINGLE CRYSTAL

Figure 7(a) exhibits the resistivity $[\rho(T)]$ curve of β-MoB_2 single crystal in the absence of an applied magnetic field.

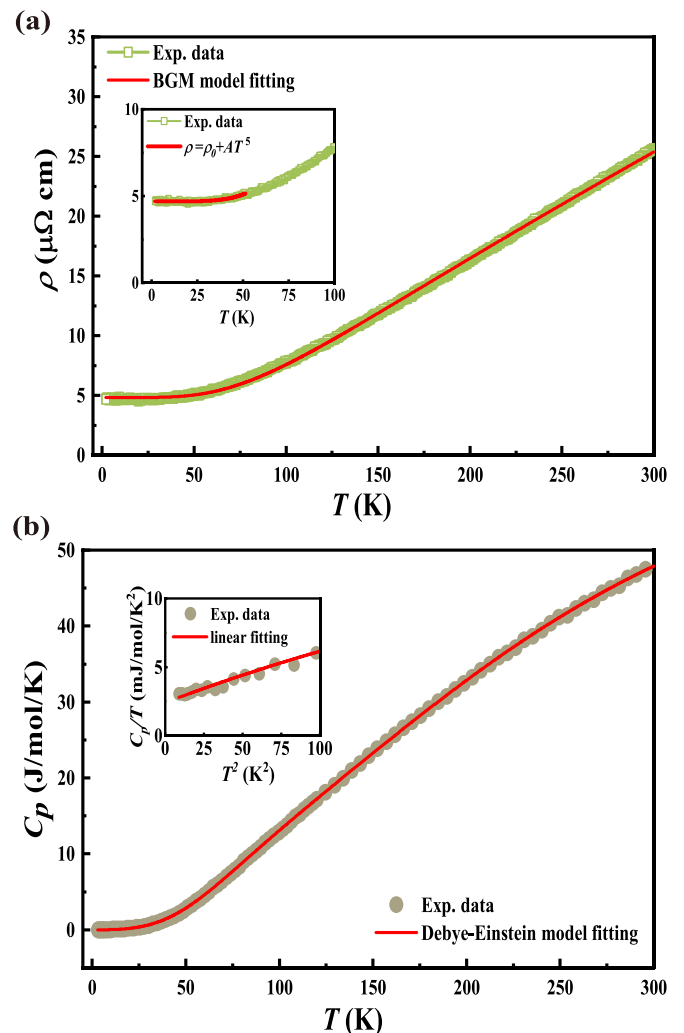FIG. 7. (a) Temperature-dependent resistivity with current flowing in the *ab* plane. The red solid is the fitted result by using the BGM model. The set is the low-temperature resistivity fitted by $\rho(T) = \rho_0 + AT^5$. (b) Specific heat vs temperature, the red solid line is the fitting to the Debye-Einstein model. The inset is the C_P/T as a function of T^2, fitted by $C_p(T)/T = \gamma_s + \beta T^2$.
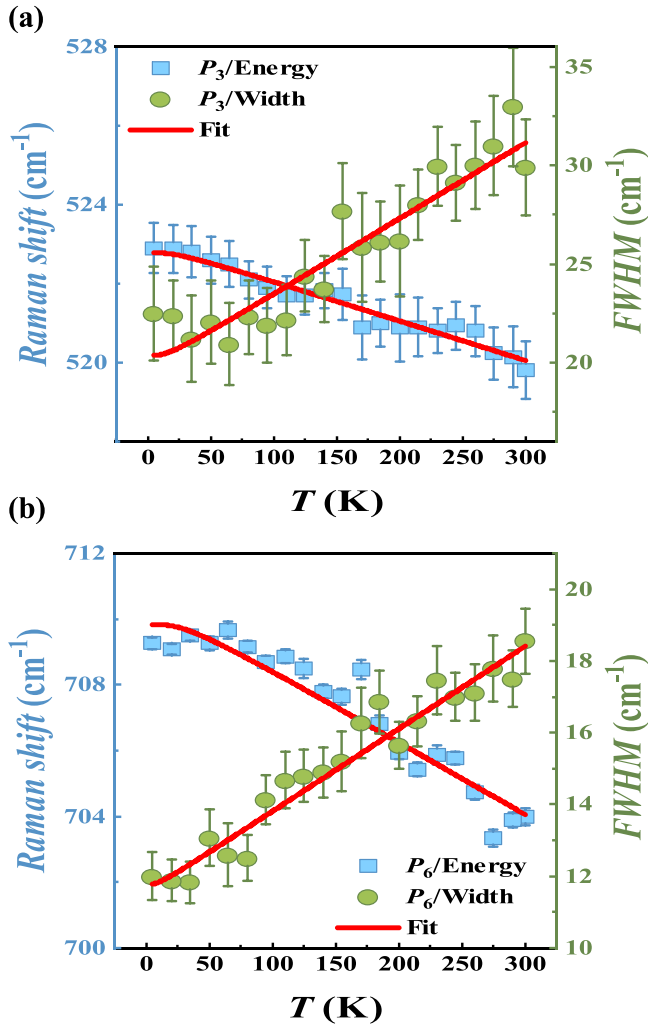
(a)

(b)

FIG. 8. Peak position and FWHM of (a) P_3 and (b) P_6 as a function of temperature. The solid line is the fitted result according to Eqs. (B1) and (B2).

It is clear that β-MoB$_2$ shows typical metallic behavior over the whole temperature range and the residual resistivity ratio [$RRR = \rho_{xx}(300\,\text{K})/\rho_{xx}(2\,\text{K})$] is about 5. The $\rho(T)$ curve over the full temperature range was fitted by Bloch-Grüneisen-Mott (BGM) model [62],

$$\rho(T) = \rho_0 + 4\Re T\left(\frac{T}{\Theta_D}\right)^4 \int_0^{\Theta_D/T} \frac{x^5}{(e^x-1)(1-e^{-x})}dx, \tag{A1}$$

where ρ_0 is residual resistivity, $\Re$ is the fitting parameter, and Θ_D is Debye temperature. The fitted ρ_0 and Θ_D is 4.67 µΩ cm and 476.9 K, respectively. This good fitting suggests that transport properties of β-MoB$_2$ are dominated by electron-phonon scattering [63]. In addition, the curve below 50 K was further fitted to the formula $\rho(T) = \rho_0 + AT^5$, as shown in the inset of Fig. 7(a), which was ever applied to fit the resistivity curve of HfB$_2$ [14], indicating electron-phonon scattering cannot be disregarded even at low temperature. The residual resistivity ρ_0 and parameter A are found to be 4.67 µΩ cm and 1.35×10^{-9} µΩ cm K^{-5}, respectively.

The zero-field specific heat with various temperature [$C_p(T)$] is pictured in Fig. 7(b). $C_p(T)$ monotonically
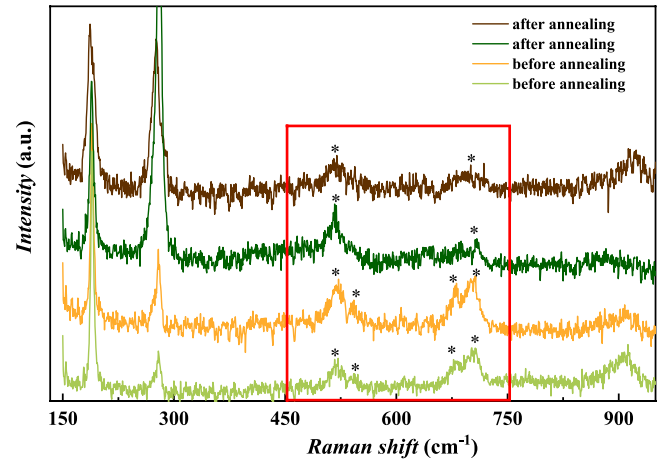

FIG. 9. The Raman spectra of β-MoB$_2$ single crystals before and after annealing.

increases as temperature rises and does not approach saturation until room temperature, indicating the energy of phonons is relatively high in β-MoB$_2$. This behavior can be explained by the existence of light B atoms in β-MoB$_2$. Here, we chose Debye-Einstein model [64] to fit the data:

$$C_p(T) = mC_D(T) + (1-m)C_E(T), \tag{A2}$$

$$C_D(T) = 9nR\left(\frac{T}{T_D}\right)^3 \int_0^{T_D/T} \frac{x^4}{(e^x-1)(1-e^{-x})}dx, \tag{A3}$$

$$C_E(T) = 3nR\left(\frac{T_E}{T}\right)^2 \frac{1}{(e^{T_E/T}-1)(1-e^{-T_E/T})}, \tag{A4}$$

where m is weighing factor which represents acoustic phonons contribution, n is the number of atoms per unit cell, R is universal gas constant, and T_D and T_E are Debye and Einstein temperature, respectively. The data can be well described with the following parameters: $m = 0.42$, $T_D = 468$ K, and $T_E = 950$ K. The Debye temperature is roughly in agreement with the value from above transport measurement. A plot of low-temperature C_p/T vs T^2 is depicted in the
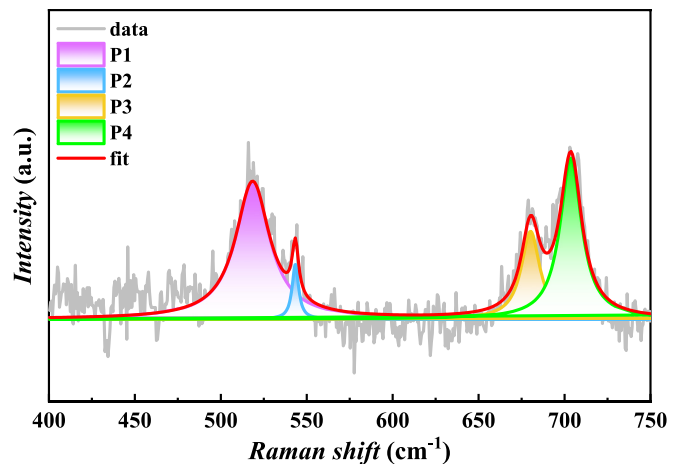

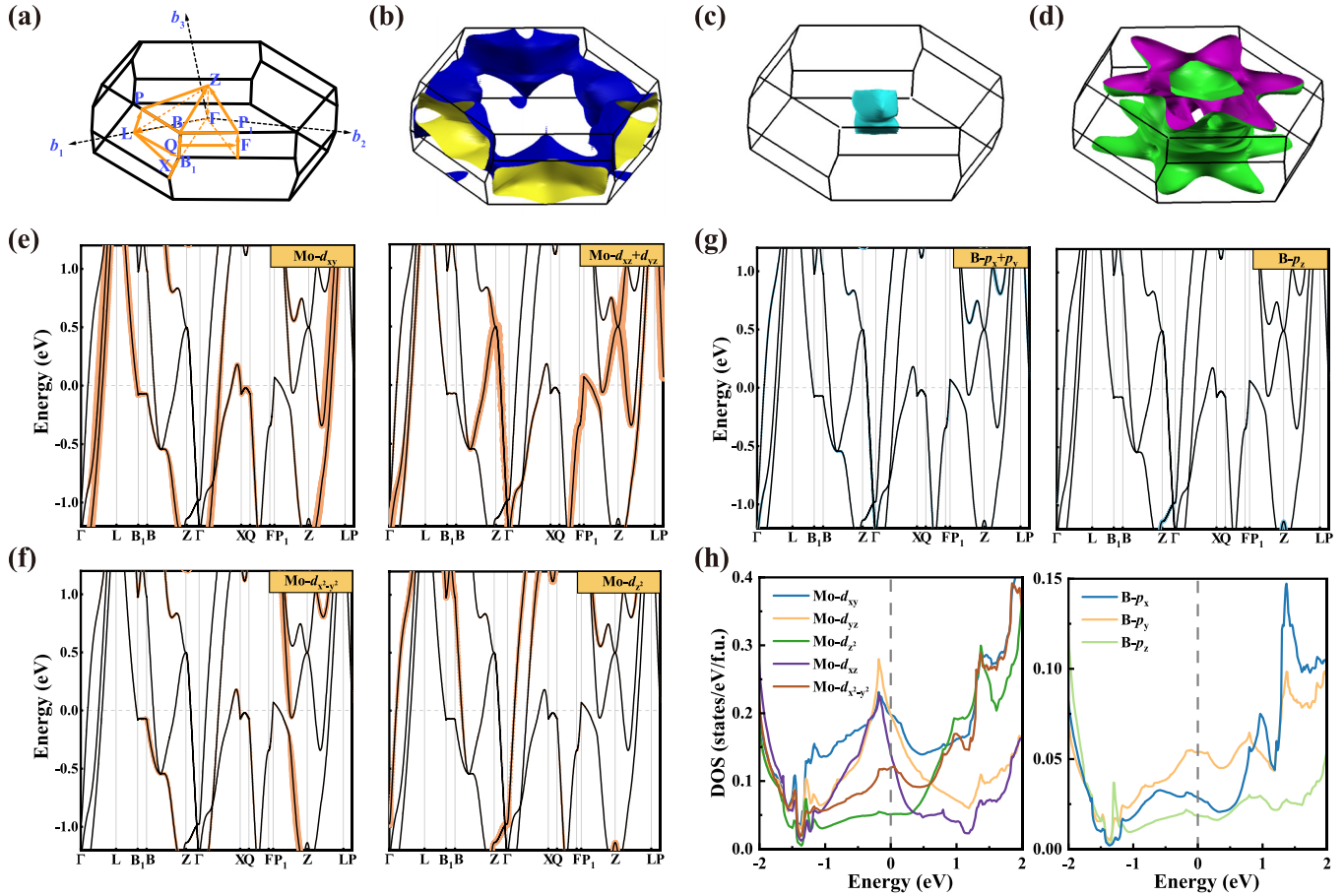FIG. 10. The multipeak fitting results of the Raman spectra for β-MoB$_2$ single crystals.

FIG. 11. (a) The BZ of β-MoB$_2$, where b_1, b_2, and b_3 are the reciprocal basis of the primitive cell. The high-symmetry path was denoted by yellow line. (b)–(d) Fermi surface of β-MoB$_2$. Orbital-resolved band structure for (e), (f) Mo and (g) B. The Fermi energy has been set to zero. (h) Orbital-resolved DOS.

inset of Fig. 7(b), which can be fitted well using the formula $C_p(T)/T = \gamma_s + \beta T^2$ with the Sommerfeld coefficient $\gamma_s = 2.6(1)$ mJ mol^{-1} K^{-2} and phonon specific-heat coefficient $\beta = 0.035$ mJ mol^{-1} K^{-4}. The relatively low value of γ_s was also observed in other diborides [65,66] and the density of states (DOS) of β-MoB$_2$ at the Fermi level [$N(E_F)$] can be evaluated using the relationship $N(E_F) = 3\gamma/\pi^2 k_B^2$. This value was calculated to be 1.1 states/eV per formula unit (f.u.).

APPENDIX B: PHONON ANHARMONICITY OF β-MoB$_2$ SINGLE CRYSTAL

In general, the peak position and FWHM correspond to the phonon energy and the phonon linewidth, respectively. The temperature-dependent phonon energy can be described as [67,68] $\omega(T) = \omega_0 + \omega_{t-e}(T) + \omega_{p-p}(T)$, where ω_0 represents the phonon energy at 0 K, $\omega_{t-e}(T)$ represents the contribution from thermal expansion, and $\omega_{p-p}(T)$ represents the effects of phonon-phonon interactions. On the other hand, the temperature-dependent phonon linewidth can be expressed as $\Gamma(T) = \Gamma_0 + \Gamma_{p-p}(T) + \Gamma_{e-p}(T)$, where Γ_0 represents the temperature-independent impurity effect, $\Gamma_{p-p}(T)$ represents the multiphonon processes resulting from phonon-phonon interactions, and $\Gamma_{e-p}(T)$ accounts for the electron-phonon

interaction, which is only applicable in the case of topological semimetals [69]. Considering that β-MoB$_2$ exhibits a layered structure, we assume that phonon-phonon interactions play a dominant role in the observed effects [70–73]. Hence, $\omega(T)$ and $\Gamma(T)$ follow these two expressions, respectively:

$$\omega(T) = \omega_0 - C\left(1 + \frac{2}{e^{\frac{\hbar\omega_0}{2k_BT}} - 1}\right), \tag{B1}$$

$$\Gamma(T) = \Gamma_0 + D\left(1 + \frac{2}{e^{\frac{\hbar\omega_0}{2k_BT}} - 1}\right), \tag{B2}$$

where C and D are positive temperature parameters, k_B is Boltzmann constant, $\hbar$ is Planck's constant. As demonstrated by the fitting results in Figs. 8(a) and 8(b), the aforementioned equations accurately describe the observed data, affirming that the temperature-dependent variations in phonon energy and linewidth are primarily attributed to phonon-phonon interactions.

APPENDIX C: SUPPLEMENTARY RAMAN RESULTS

To confirm whether the peak splitting is induced by lattice defects, we subjected the single crystal to anneal at 900 °C in order to minimize the local lattice distortions caused by defects. As shown in Fig. 9, we measured the Raman spectra
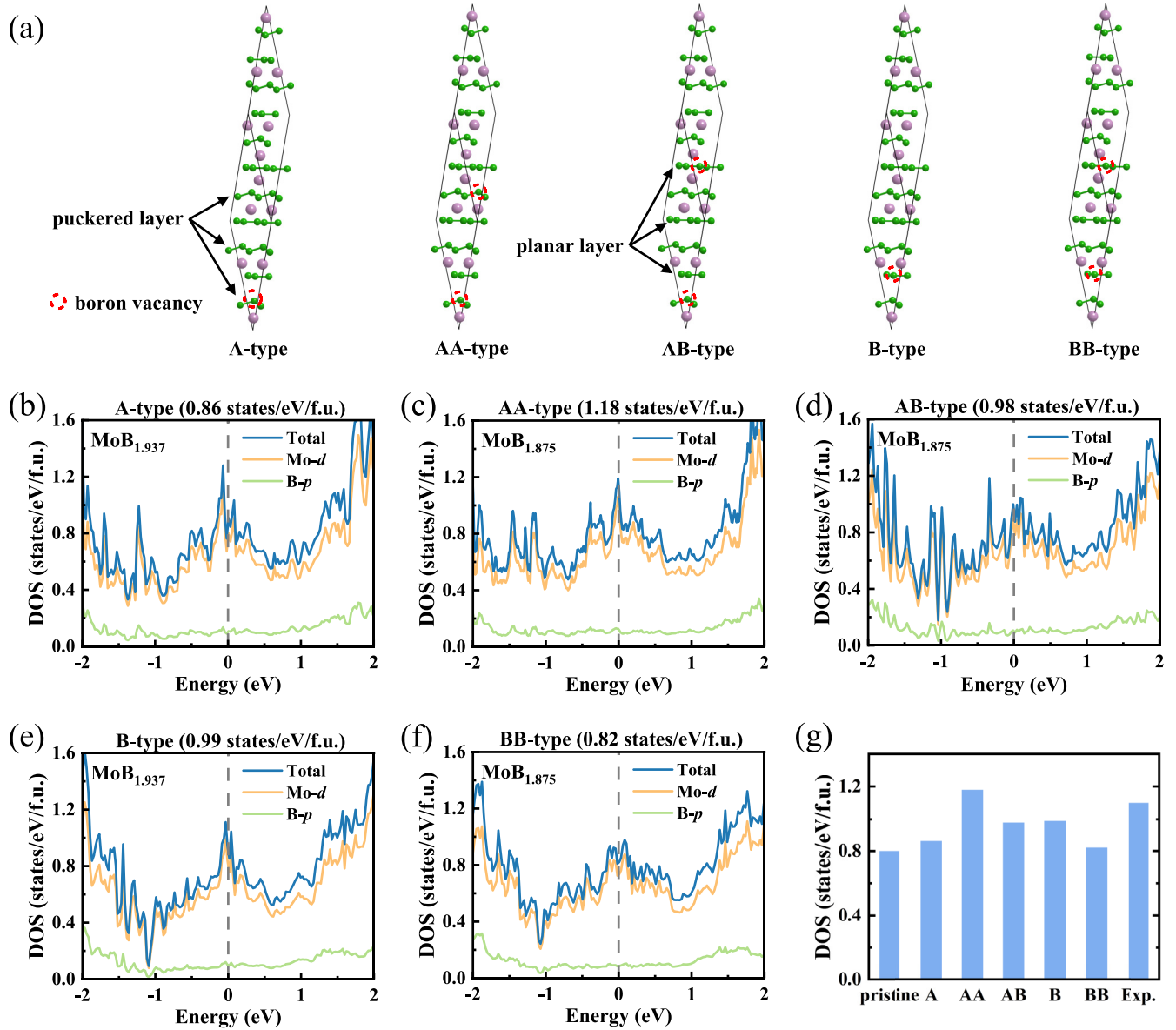
FIG. 12. (a) β-MoB$_2$ with different types of boron vacancies. Red circles indicate the boron vacancies. (b)–(f) DOS of β-MoB$_2$ with different vacancy types. (g) Summary of DOS at Fermi level.

of two single crystal before and after annealing. The range of peak splitting is indicated by a red box, and the splitted peaks are marked with asterisks (*).

Figure 10 and Table II show the multipeak fitting results of the Raman spectra for β-MoB$_2$ single crystals.

TABLE II. Parameter table of multipeak fitting results.

Peak index	Peak type	Area intg.
1	Lorentz	3399.09355
2	Lorentz	265.74506
3	Lorentz	1203.38913
4	Lorentz	2493.22569

APPENDIX D: ELECTRONIC STRUCTURE CALCULATIONS

Figure 11(a) schematically illustrates the BZ of β-MoB$_2$, highlighting the high-symmetry points and paths in orange. Figures 11(b)–11(d) display the Fermi surface of bulk β-MoB$_2$ without considering spin-orbit coupling, revealing the presence of two large and one small three-dimensional (3D) sheets. Figures 11(e)–11(g) illustrate the band structure, where the projected bands with spectral weight originating from Mo d_{xy}, $d_{xz} + d_{yz}$, $d_{x^2+y^2}$, and d_{z^2} orbitals are depicted in orange, while the B $p_x + p_y$ and p_z orbitals orbitals are shown in blue. Additionally, Fig. 11(h) illustrates the corresponding partial DOS, which clearly indicates that the electronic states

crossing the Fermi level are predominantly contributed by the $3d$ orbitals of Mo atoms.

The calculated DOS of β-MoB$_2$ is 0.8 states/eV/f.u., which is smaller than our experimental value of 1.1 states/eV/f.u. We attribute this difference to the presence of lattice defects in our experiments. Here, we considered the effects of boron vacancies and calculated the DOS of β-MoB$_{2-\delta}$ using a $2 \times 2 \times 2$ supercell with different boron vacancies. The summary of the results is shown in Fig. 12.

In β-MoB$_2$, boron vacancies can be located in two different boron atom layers: the puckered layer and the planar layer. Here, we considered five vacancy configurations, and the vacancy sites are located as far as possible from each other in the lattice [see Fig. 12(a)]. Figure 12 shows the DOS of β-MoB$_2$ with a boron vacancy in a puckered layer, denoted A-type. Compared with the pristine β-MoB$_2$, the Fermi level in Fig. 12(b) is closer to the peak of DOS, resulting in a slight increase of DOS to the 0.86 states/eV/f.u. Upon introducing a second boron vacancy in another puckered layer (AA-type), the Fermi level is moved to the peak of DOS [see Fig. 12(c)], significantly enhancing the DOS to 1.18 states/eV/f.u., which is closer to our experimental value.

The DOS of one boron vacancy in the planar layer (B-type) is displayed in Fig. 12(e). The Fermi level also shows movement to the peak, resulting in the enhanced DOS of 0.99 states/eV/f.u. For the structure containing two boron vacancies in planar layers (BB-type), the peak value decreases. Consequently, the BB-type has a DOS of 0.82 states/eV/f.u. Figure 12(d) shows boron vacancies in both the puckered and planar layers (AB-type), with a DOS of 0.98 states/eV/f.u. In conclusion, the presence of boron vacancies could enhance the DOS at the Fermi level. Especially for the AA-type, which shows higher DOS value close to our experimental one.

[1] J. Nagamatsu, N. Nakagawa, T. Muranaka, Y. Zenitani, and J. Akimitsu, Superconductivity at 39 K in magnesium diboride, Nature (London) **410**, 63 (2001).

[2] M. Tomsic, M. Rindfleisch, J. Yue, K. McFadden, J. Phillips, M. D. Sumption, M. Bhatia, S. Bohnenstiehl, and E. W. Collings, Overview of MgB$_2$ superconductor applications, Int. J. Appl. Ceram. Technol. **4**, 250 (2007).

[3] N. I. Medvedeva, A. L. Ivanovskii, J. E. Medvedeva, and A. J. Freeman, Electronic structure of superconducting MgB$_2$ and related binary and ternary borides, Phys. Rev. B **64**, 020502(R) (2001).

[4] Z. Yu, T. Bo, B. Liu, Z. Fu, H. Wang, S. Xu, T. Xia, S. Li, S. Meng, and M. Liu, Superconductive materials with MgB$_2$-like structures from data-driven screening, Phys. Rev. B **105**, 214517 (2022).

[5] J. E. Schirber, D. L. Overmyer, B. Morosin, E. L. Venturini, R. Baughman, D. Emin, H. Klesnar, and T. Aselage, Pressure dependence of the superconducting transition temperature in single-crystal NbB$_x$ (x near 2) with $T_c = 9.4$ K, Phys. Rev. B **45**, 10787 (1992).

[6] S. M. Sichkar and V. N. Antonov, Electronic structure, phonon spectra and electron–phonon interaction in ScB$_2$, Low Temp. Phys. **39**, 595 (2013).

[7] X. Zhang, Z.-M. Yu, X.-L. Sheng, H. Y. Yang, and S. A. Yang, Coexistence of four-band nodal rings and triply degenerate nodal points in centrosymmetric metal diborides, Phys. Rev. B **95**, 235116 (2017).

[8] X. Feng, C. Yue, Z. Song, Q. Wu, and B. Wen, Topological Dirac nodal-net fermions in AlB$_2$-type TiB$_2$ and ZrB$_2$, Phys. Rev. Mater. **2**, 014202 (2018).

[9] D. Takane, S. Souma, K. Nakayama, T. Nakamura, H. Oinuma, K. Hori, K. Horiba, H. Kumigashira, N. Kimura, T. Takahashi, and T. Sato, Observation of a Dirac nodal line in AlB$_2$, Phys. Rev. B **98**, 041105(R) (2018).

[10] Z. Liu, R. Lou, P. Guo, Q. Wang, S. Sun, C. Li, S. Thirupathaiah, A. Fedorov, D. Shen, K. Liu, H. Lei, and S.

[11] Wang, Experimental observation of dirac nodal links in centrosymmetric semimetal TiB$_2$, Phys. Rev. X **8**, 031044 (2018).

C.-J. Yi, B. Q. Lv, Q. S. Wu, B.-B. Fu, X. Gao, M. Yang, X.-L. Peng, M. Li, Y.-B. Huang, P. Richard, M. Shi, G. Li, O. V. Yazyev, Y.-G. Shi, T. Qian, and H. Ding, Observation of a nodal chain with Dirac surface states in TiB$_2$, Phys. Rev. B **97**, 201107(R) (2018).

[12] R. Lou, P. Guo, M. Li, Q. Wang, Z. Liu, S. Sun, C. Li, X. Wu, Z. Wang, Z. Sun *et al.*, Experimental observation of bulk nodal lines and electronic surface states in ZrB$_2$, npj Quantum Mater. **3**, 50 (2018).

[13] Q. Wang, P.-J. Guo, S. Sun, C. Li, K. Liu, Z.-Y. Lu, and H. Lei, Extremely large magnetoresistance and high-density Dirac-like fermions in ZrB$_2$, Phys. Rev. B **97**, 205105 (2018).

[14] Q. Wang, Q. Yin, and H. Lei, Magnetotransport properties of compensated semimetal HfB$_2$ with high-density light carriers, J. Phys.: Condens. Matter **32**, 015601 (2020).

[15] H. Meng, B. Li, Z. Han, Y. Zhang, X. Wang, and Z. Zhang, Reversible magnetocaloric effect and refrigeration capacity enhanced by two successive magnetic transitions in DyB$_2$, Sci. China: Technol. Sci. **55**, 501 (2012).

[16] N. Terada, K. Terashima, P. B. de Castro, C. V. Colin, H. Mamiya, T. D. Yamamoto, H. Takeya, O. Sakai, Y. Takano, and H. Kitazawa, Relationship between magnetic ordering and gigantic magnetocaloric effect in HoB$_2$ studied by neutron diffraction experiment, Phys. Rev. B **102**, 094435 (2020).

[17] W. Yang, G. Xiao, Q. Zhu, Y. Cui, S. Song, G.-H. Cao, and Z. Ren, Stabilization and superconductivity of AlB$_2$-type nonstoichiometric molybdenum diboride by Sc doping, Ceram. Int. **48**, 19971 (2022).

[18] T. T. Zhang, H. Miao, Q. Wang, J. Q. Lin, Y. Cao, G. Fabbris, A. H. Said, X. Liu, H. C. Lei, Z. Fang, H. M. Weng, and M. P. M. Dean, Phononic helical nodal lines with $\mathcal{PT}$ protection in MoB$_2$, Phys. Rev. Lett. **123**, 245302 (2019).

[19] J. Li, J. Liu, S. A. Baronett, M. Liu, L. Wang, R. Li, Y. Chen, D. Li, Q. Zhu, and X.-Q. Chen, Computation and data driven

discovery of topological phononic materials, Nat. Commun. **12**, 1204 (2021).

[20] C. Pei, J. Zhang, Q. Wang, Y. Zhao, L. Gao, C. Gong, S. Tian, R. Luo, M. Li, W. Yang, Z.-Y. Lu, H. Lei, K. Liu, and Y. Qi, Pressure-induced superconductivity at 32 K in MoB_2, Natl. Sci. Rev. **10**, nwad034 (2023).

[21] Y. Quan, K.-W. Lee, and W. E. Pickett, MoB_2 under pressure: Superconducting Mo enhanced by boron, Phys. Rev. B **104**, 224504 (2021).

[22] X. Liu, X. Huang, P. Song, C. Wang, L. Zhang, P. Lv, L. Liu, W. Zhang, J.-H. Cho, and Y. Jia, Strong electron-phonon coupling superconductivity in compressed $\alpha-MoB_2$ induced by double van Hove singularities, Phys. Rev. B **106**, 064507 (2022).

[23] L. E. Muzzy, M. Avdeev, G. Lawes, M. K. Haas, H. W. Zandbergen, A. P. Ramirez, J. D. Jorgensen, and R. J. Cava, Structure and superconductivity in Zr-stabilized, nonstoichiometric molybdenum diboride, Physica C (Amsterdam, Neth.) **382**, 153 (2002).

[24] A. C. Hire, S. Sinha, J. Lim, J. S. Kim, P. M. Dee, L. Fanfarillo, J. J. Hamlin, R. G. Hennig, P. J. Hirschfeld, and G. R. Stewart, High critical field superconductivity at ambient pressure in MoB_2 stabilized in the P6/mmm structure via Nb substitution, Phys. Rev. B **106**, 174515 (2022).

[25] N. Lazarević, E. S. Bozin, M. Šćepanović, M. Opačić, H. Lei, C. Petrovic, and Z. V. Popović, Probing $IrTe_2$ crystal symmetry by polarized Raman scattering, Phys. Rev. B **89**, 224301 (2014).

[26] P. Soubelet, A. E. Bruchhausen, A. Fainstein, K. Nogajewski, and C. Faugeras, Resonance effects in the Raman scattering of monolayer and few-layer $MoSe_2$, Phys. Rev. B **93**, 155407 (2016).

[27] C. Lee, H. Yan, L. E. Brus, T. F. Heinz, J. Hone, and S. Ryu, Anomalous lattice vibrations of single- and few-layer MoS_2, ACS Nano **4**, 2695 (2010).

[28] U. D. Wdowik, G. Jagło, and D. Legut, Effect of cation-vacancy superstructure on the phonon dynamics in KNi_2Se_2, Phys. Rev. B **101**, 045125 (2020).

[29] V. K. Veerapandiyan, S. Khosravi, G. Canu, A. Feteira, V. Buscaglia, K. Reichmann, and M. Deluca, B-site vacancy induced Raman scattering in $BaTiO_3$-based ferroelectric ceramics, J. Eur. Ceram. Soc. **40**, 4684 (2020).

[30] C. Lee, B. G. Jeong, S. H. Kim, D. H. Kim, S. J. Yun, W. Choi, S.-J. An, D. Lee, Y.-M. Kim, K. K. Kim *et al.*, Investigating heterogeneous defects in single-crystalline WS_2 via tip-enhanced Raman spectroscopy, npj 2D Mater. Appl. **6**, 67 (2022).

[31] Y. Zhang, L. Yan, W. Wu, G. He, J. Zhang, Z. Ni, X. Jiang, M. Qin, F. Jin, J. Yuan, B. Zhu, Q. Chen, L. Zhou, Y. Li, J. Luo, and K. Jin, Single-crystalline transition metal phosphide superconductor WP studied by Raman spectroscopy and first-principles calculations, Phys. Rev. B **105**, 174511 (2022).

[32] W.-L. Zhang, H. Li, D. Xia, H. W. Liu, Y.-G. Shi, J. L. Luo, J. Hu, P. Richard, and H. Ding, Observation of a Raman-active phonon with Fano line shape in the quasi-one-dimensional superconductor $K_2Cr_3As_3$, Phys. Rev. B **92**, 060502(R) (2015).

[33] D. Chen, Y.-L. Jia, T.-T. Zhang, Z. Fang, K. Jin, P. Richard, and H. Ding, Raman study of electron-phonon coupling in thin films of the spinel oxide superconductor $LiTi_2O_4$, Phys. Rev. B **96**, 094501 (2017).

[34] Y. Hu, F. Zheng, X. Ren, J. Feng, and Y. Li, Charge density waves and phonon-electron coupling in $ZrTe_3$, Phys. Rev. B **91**, 144502 (2015).

[35] B. Lyu, L. Wang, Y. Gao, S. Guo, X. Zhou, Z. Hao, S. Wang, Y. Zhao, L. Huang, J. Shao, and M. Huang, Structural and magnetic phase transitions in quasi-two-dimensional VBr_3, Phys. Rev. B **106**, 085430 (2022).

[36] M. Hünermann, J. Geurts, and W. Richter, Observation of interface phonons by light scattering from epitaxial Sb monolayers on III-V semiconductors, Phys. Rev. Lett. **66**, 640 (1991).

[37] H.-H. Kung, M. Salehi, I. Boulares, A. F. Kemper, N. Koirala, M. Brahlek, P. Lošťák, C. Uher, R. Merlin, X. Wang, S.-W. Cheong, S. Oh, and G. Blumberg, Surface vibrational modes of the topological insulator Bi_2Se_3 observed by Raman spectroscopy, Phys. Rev. B **95**, 245406 (2017).

[38] M. Denk, E. Speiser, J. Plaickner, S. Chandola, S. Sanna, P. Zeppenfeld, and N. Esser, Surface resonant raman scattering from Cu(110), Phys. Rev. Lett. **128**, 216101 (2022).

[39] S. Okada, T. Atoda, I. Higashi, and Y. Takahashi, Preparation of single crystals of MoB_2 by the aluminium-flux technique and some of their properties, J. Mater. Sci. **22**, 2993 (1987).

[40] J. Rodríguez-Carvajal, Recent advances in magnetic structure determination by neutron powder diffraction, Physica B (Amsterdam, Neth.) **192**, 55 (1993).

[41] G. Kresse and J. Hafner, Ab initio molecular dynamics for liquid metals, Phys. Rev. B **47**, 558 (1993).

[42] P. E. Blöchl, Projector augmented-wave method, Phys. Rev. B **50**, 17953 (1994).

[43] J. P. Perdew, K. Burke, and M. Ernzerhof, Generalized gradient approximation made simple, Phys. Rev. Lett. **77**, 3865 (1996).

[44] A. Togo and I. Tanaka, First principles phonon calculations in materials science, Scr. Mater. **108**, 1 (2015).

[45] P. Giannozzi, S. Baroni, N. Bonini, M. Calandra, R. Car, C. Cavazzoni, D. Ceresoli, G. L. Chiarotti, M. Cococcioni, I. Dabo *et al.*, Quantum espresso: A modular and open-source software project for quantum simulations of materials, J. Phys.: Condens. Matter **21**, 395502 (2009).

[46] M. Guc, S. Levcenko, I. V. Bodnar, V. Izquierdo-Roca, X. Fontane, L. V. Volkova, E. Arushanov, and A. Pérez-Rodríguez, Polarized Raman scattering study of kesterite type Cu_2ZnSnS_4 single crystals, Sci. Rep. **6**, 19414 (2016).

[47] H. Zobeiri, R. Wang, C. Deng, Q. Zhang, and X. Wang, Polarized Raman of nanoscale two-dimensional materials: Combined optical and structural effects, J. Phys. Chem. C **123**, 23236 (2019).

[48] K. Nagai, K. Uchida, S. Kusaba, T. Endo, Y. Miyata, and K. Tanaka, Effect of incoherent electron-hole pairs on high harmonic generation in an atomically thin semiconductor, Phys. Rev. Res. **5**, 043130 (2023).

[49] W. L. McMillan, Transition temperature of strong-coupled superconductors, Phys. Rev. **167**, 331 (1968).

[50] W. H. Weber and R. Merlin, *Raman Scattering in Materials Science* (Springer Berlin, Heidelberg, 2000), Vol. 42.

[51] N. Khossossi, D. Singh, A. Ainane, and R. Ahuja, Recent progress of defect chemistry on 2D materials for advanced battery anodes, Chem. - Asian J. **15**, 3390 (2020).

[52] X.-L. Liu, X. Zhang, M.-L. Lin, and P.-H. Tan, Different angle-resolved polarization configurations of Raman spectroscopy: A case on the basal and edge plane of two-dimensional materials, Chin. Phys. B **26**, 067802 (2017).

[53] V. G. Hadjiev, M. N. Iliev, B. Lv, Z. F. Ren, and C. W. Chu, Anomalous vibrational properties of cubic boron arsenide, Phys. Rev. B **89**, 024308 (2014).

[54] J. S. Kang, M. Li, H. Wu, H. Nguyen, and Y. Hu, Experimental observation of high thermal conductivity in boron arsenide, Science **361**, 575 (2018).

[55] M. Da, C. Xin, L. Yu-Chen, L. Miao-Ling, W. Jia-Hong, Y. Bin-Lu, L. Xue-Lu, Y. Xue-Feng, and T. Ping-Heng, Resonant multi-phonon Raman scattering of black phosphorus, Acta Phys. Sin. **69**, 167803 (2020).

[56] S. Pei, J. Tang, C. Liu, J.-W. Mei, Z. Guo, B. Lyu, N. Zhang, Q. Huang, D. Yu, L. Huang *et al.*, Orbital-fluctuation freezing and magnetic-nonmagnetic phase transition in α-TiBr$_3$, Appl. Phys. Lett. **117**, 133103 (2020).

[57] M. Xie, B. Winkler, Z. Mao, R. B. Kaner, A. Kavner, and S. H. Tolbert, Raman scattering from superhard rhenium diboride under high pressure, Appl. Phys. Lett. **104**, 011904 (2014).

[58] J. Hlinka, I. Gregora, J. Pokorný, A. Plecenik, P. Kúš, L. Satrapinsky, and Š Beňačka, Phonons in MgB$_2$ by polarized Raman scattering on single crystals, Phys. Rev. B **64**, 140503(R) (2001).

[59] S. Zhao, M. Lu, S. Xue, L. Yan, P. Miao, Y. Hang, X. Wang, Z. Liu, Y. Wang, L. Tao *et al.*, A Se vacancy induced localized Raman mode in two-dimensional MoSe$_2$ grown by CVD, arXiv:1904.09789.

[60] J. Lim, A. C. Hire, Y. Quan, J. S. Kim, S. R. Xie, S. Sinha, R. S. Kumar, D. Popov, C. Park, R. J. Hemley *et al.*, Creating superconductivity in WB$_2$ through pressure-induced metastable planar defects, Nat. Commun. **13**, 7901 (2022).

[61] C. Pei, J. Zhang, C. Gong, Q. Wang, L. Gao, Y. Zhao, S. Tian, W. Cao, C. Li, Z.-Y. Lu *et al.*, Distinct superconducting behaviors of pressurized WB$_2$ and ReB$_2$ with different local B layers, Sci. China: Phys., Mech. Astron. **65**, 287412 (2022).

[62] J. Gao, J. G. Si, X. Luo, J. Yan, Z. Z. Jiang, W. Wang, C. Q. Xu, X. F. Xu, P. Tong, W. H. Song *et al.*, Superconducting and topological properties in centrosymmetric PbTaS$_2$ single crystals, J. Phys. Chem. C **124**, 6349 (2020).

[63] J. M. Ziman, *Electrons and Phonons* (Clarendon Press, Oxford, 1960).

[64] J. Maiwald and M. C. Aronson, Physical and one-dimensional properties of single-crystalline La$_5$AgPb$_3$, Phys. Rev. B **105**, 155116 (2022).

[65] S. T. Renosto, H. Consoline, C. A. M. dos Santos, J. Albino Aguiar, S.-G. Jung, J. Vanacken, V. V. Moshchalkov, Z. Fisk, and A. J. S. Machado, Evidence of multiband behavior in the superconducting alloy Zr$_{0.96}$V$_{0.04}$B$_2$, Phys. Rev. B **87**, 174502 (2013).

[66] S. T. Renosto, R. Lang, E. Diez, L. E. Corrêa, M. S. da Luz, Z. Fisk, and A. J. S. Machado, Evidence of unconventional superconductivity in the Ni-doped NbB$_2$ system, J. Alloys Compd. **787**, 414 (2019).

[67] R. Singha, S. Samanta, S. Chatterjee, A. Pariari, D. Majumdar, B. Satpati, L. Wang, A. Singha, and P. Mandal, Probing lattice dynamics and electron-phonon coupling in the topological nodal-line semimetal ZrSiS, Phys. Rev. B **97**, 094112 (2018).

[68] H.-M. Eiter, P. Jaschke, R. Hackl, A. Bauer, M. Gangl, and C. Pfleiderer, Raman study of the temperature and magnetic-field dependence of the electronic and lattice properties of MnSi, Phys. Rev. B **90**, 024411 (2014).

[69] A. C. Ferrari, Raman spectroscopy of graphene and graphite: disorder, electron–phonon coupling, doping and nonadiabatic effects, Solid State Commun. **143**, 47 (2007).

[70] P. G. Klemens, Anharmonic decay of optical phonons, Phys. Rev. **148**, 845 (1966).

[71] J. Menéndez and M. Cardona, Temperature dependence of the first-order Raman scattering by phonons in Si, Ge, and α-Sn: Anharmonic effects, Phys. Rev. B **29**, 2051 (1984).

[72] W.-D. Kong, S.-F. Wu, P. Richard, C.-S. Lian, J.-T. Wang, C.-L. Yang, Y.-G. Shi, and H. Ding, Raman scattering investigation of large positive magnetoresistance material WTe$_2$, Appl. Phys. Lett. **106**, 081906 (2015).

[73] J. J. Gao, J. G. Si, X. Luo, J. Yan, F. C. Chen, G. T. Lin, L. Hu, R. R. Zhang, P. Tong, W. H. Song, X. B. Zhu, W. J. Lu, and Y. P. Sun, Origin of the structural phase transition in single-crystal TaTe$_2$, Phys. Rev. B **98**, 224104 (2018).